Mechanosensory representation of wing deformations

Authors: Alexandra M. Yarger[1], Masateru Maeda[2], Igor Siwanowicz[3], Haruhiro Kajiyama[2], Simon M. Walker[4], Richard J. Bomphrey[5], & Huai-Ti Lin[1]

Corresponding authors: a.yarger@imperial.ac.uk, h.lin@imperial.ac.uk

Keywords: mechanosensation, deformation, flexible wing, dragonfly, flight, aeroelasticity, finite element modelling, digital image correlation

Author Affiliations:
[1]Department of Bioengineering, Imperial College London, UK.
[2]Graduate School of Engineering, Takushoku University, Japan.
[3]HHMI Janelia Research Campus, USA.
[4]School of Biomedical Sciences, University of Leeds, UK.
[5]Department of Comparative Biomedical Sciences, Royal Veterinary College, UK.

Abstract

Efficient representation of structural deformations is crucial for monitoring the instantaneous state of biological structures. Insects' ability to encode wing deformations during flight demonstrates a general morphological computing principle applicable across sensory systems in nature as well as engineered systems. To characterize how relevant features are encoded, we measured and modelled displacement and strain across dragonfly wing surfaces in tethered and free flight. Functional interpretations were supported by neuroanatomical maps, and ablation and perturbation experiments. We find that signal redundancy is reduced by non-random sensor distributions and that morphology limits the stimulus space such that sensory systems can monitor natural states with few sensors. Deviations from the natural states are detected by a flexible population of additional sensors with many distinguishable activation patterns.

Introduction

All organisms, even single cells, react to touch[1]. Mechanosensation is one of the most basic senses, yet there is remarkable diversity in the types of information detectable through physical forces. The specificity of sensory systems is essential for behaviour, but it is energetically expensive to maintain many sensors. The nervous system also has a limit to the amount of data it can process, so computational efficiency must be maximized while still maintaining flexibility and precision. This is a challenge not only for nervous systems, but for any system that requires information processing. Robotics approaches for sensory representation typically use few high-precision sensors and require complex control systems that incur extensive computational overheads. Yet, high processing power and precise measurements are often not available and not required for biological systems. Insects for example, use many distributed, low-precision sensors that are robust and adaptable to change. Insects manage to use relatively few neurons to cope with the computational demands of producing complex behaviours[2].

Historically, insects have provided a significant source for bioinspiration in engineered technologies[3–6]. The precise tuning of their sensory systems results from their physical anatomy and efficient encoding mechanisms. Matched filters are used to extract only relevant information from the environment by limiting the responsiveness of neurons to specific inputs, thereby reducing computation further downstream. The neurophysiological tuning of sensors is linked to the natural states an animal experiences and inputs often have direct connections to the motor neurons

responsible for relevant behaviour outputs[7–11]. These salient inputs are detected by tuning the population response of many sensors or by optimising the encoding properties of individual sensors. Information is filtered further by sensory gating - where multiple modalities must be present in order for downstream neurons monitoring a particular state of the system to be activated[12,13]. During flight, gain and temporal frequency tuning can be modulated at multiple stages to allow dynamic and context-specific sensorimotor control[14–16]. However, what is less commonly considered, is that information can also be filtered *prior* to reaching the sensory interface. The stimulus space can be constrained by 'morphological computation', where inputs are filtered by structural mechanics, sensor location, or both.

Structural specificity is well documented for mechanosensation. The directional selectivity of strain sensors, for example, is often determined by structural morphology[17]. Location can also effectively filter the signal space because different regions naturally receive greater or lesser exposure to relevant inputs. Similarly, if the signal is consistent across a large area the number of sensors necessary to represent that region is reduced. Rigid structures like legs require few proprioceptors at the hinge to represent the stimulus space sufficiently, but to represent more complex deformations typically requires more sensors. A structure's mechanical behaviour can evolve or develop to reduce degrees of freedom and hence the number of sensors required for representation, but this is rarely a feasible option under the constraints of agile locomotion. However, in the context of behaviour, it isn't always necessary to represent every possible input condition constantly. Signal redundancy is common because every region of a structure is contiguous and the patterns of local mechanical states are correlated so, the encoding task can be simplified by monitoring a subset of the area, or limiting which elements of the motion are encoded.

How do we identify what and where to measure to represent the minimum necessary salient features with sufficient accuracy? First, we must describe the stimulus space, or in the case of structural deformations, the natural range of displacement and strain. Next, to remove signal redundancy, the dimensionality of the stimulus space must be reduced, and then filtered by measuring which features are encoded by the nervous system (and are therefore relevant to the production of behaviour). Finally, to identify the optimal locations for measuring these signals, we must consider how the information is detected and which regions experience the most consistently detectable relevant signals.

To test whether morphological computation is used to tune sensors in biological systems, dragonflies are an ideal model. Their large, highly deformable wings are easy for structural measurements and their wing afferent signals are accessible for electrophysiological recordings. Furthermore, while all flying animals have deformable mechanosensitive wings, dragonflies are among the most agile fliers and their wings are frequently used as models for aerodynamics and wing mechanics[18–26]. There have been many studies on dragonfly wings, yet essential detailed 3D anatomy has rarely been included with high fidelity, nor assessed in the context of free flight. From the sensory perspective, the types and distributions of mechanosensors on the wings have been identified[27], but there has been no characterisation of how they monitor the wings' deformation states. Other deformable objects from bridges to prosthetics, have been extensively studied across fields with much effort placed on the development of displacement and strain field measurement and reconstruction techniques[28–35]. Despite the advances in deformation sensing, the challenges are consistent across different applications - improving sensor robustness to damage, information encoding efficiency, and adaptability to change. A source for solutions is the dragonflies' relatively small nervous system and its ability to cope with frequent wing damage and ever-changing behavioural and environmental contexts.

The dragonfly wings' mechanics naturally limit their range of deformation, but there is a large available state space significant for flight control. To determine the primary features that describe the range of natural wing deformation, we used a multipronged approach, measuring and modelling the local and global displacement and strain across the wing surface in tethered and freely flying

dragonflies. To identify relevant deformation features within the natural range, we characterized which features were encoded, and how. For functional interpretations it is also important to consider the accuracy of the neural representation of the sensory signal. Information theory is widely used to quantify the reliability of stimulus-response functions. Here we use information content to characterize relevant spatial features in addition to describing the reliability of temporal deformation pattern encoding[36,37]. Taken together, we demonstrate a simple mechanism of morphological computation for mechanosensory encoding in a biological system. The general principle, based on insects' ability to closely monitor wing deformations during flight, is likely to be applicable across sensory systems in nature as well as offering design guidelines for inputs to artificial neural networks used to control diverse dynamic systems.

Wing deformation patterns

To understand how dragonfly (*Sympetrum striolatum*) wing sensory signals encode wing deformation we drove a fixed wing into aeroelastic flutter while recording extracellularly from the afferent nerve fibre (Figure 1A). Before modelling the signal encoding scheme, we needed to characterize the natural wing deformation patterns during flight. To achieve this, we took three parallel approaches. Firstly, a high-speed camera captured the wing deformation of a fluttering wing to measure the displacement and strain using digital image correlation (DIC; see Methods; Figure 1B). Secondly, we reconstructed natural wing deformations of dragonflies using a high-speed, nine-camera free flight arena. The synchronised and calibrated images from these cameras allowed us to reconstruct the leading and trailing edges of each wing during flight, and hence a second set of displacement maps. Finally, we produced a high-fidelity wing model incorporating fine detail of vein geometry for Finite Element Analysis (FEA; Figure 1D). A modal analysis yielded displacement and strain fields (Figure 1E) for comparison.

To characterise the natural wing deformation, we sought to represent the overall wing motion with the fewest necessary variables by dimensional reduction. A principal components analysis (PCA) across the conditions revealed that 99% of the wing motion's overall displacement variability was described by the first three PCs, interpreted as bending, twist, and camber (Figure 1E) The same modes were also present in our flapping flight measurements (Figure 1F), except for the mode representing camber, which is not currently measurable in the free flight apparatus because only the leading a trailing edge of the wing are reconstructed, but has been previously documented in free flight[38]. Nevertheless, the bend and twist modes represented 96% of the displacement variability. These are the same modes that emerged from the FEA simulation (Figure 1G), giving confidence in the sufficiency of our high-fidelity wing geometry model. Together, we show that a linear decomposition of wing displacements reveals a handful of modes inherent to the wing structure that are excited during gliding and flapping flight.

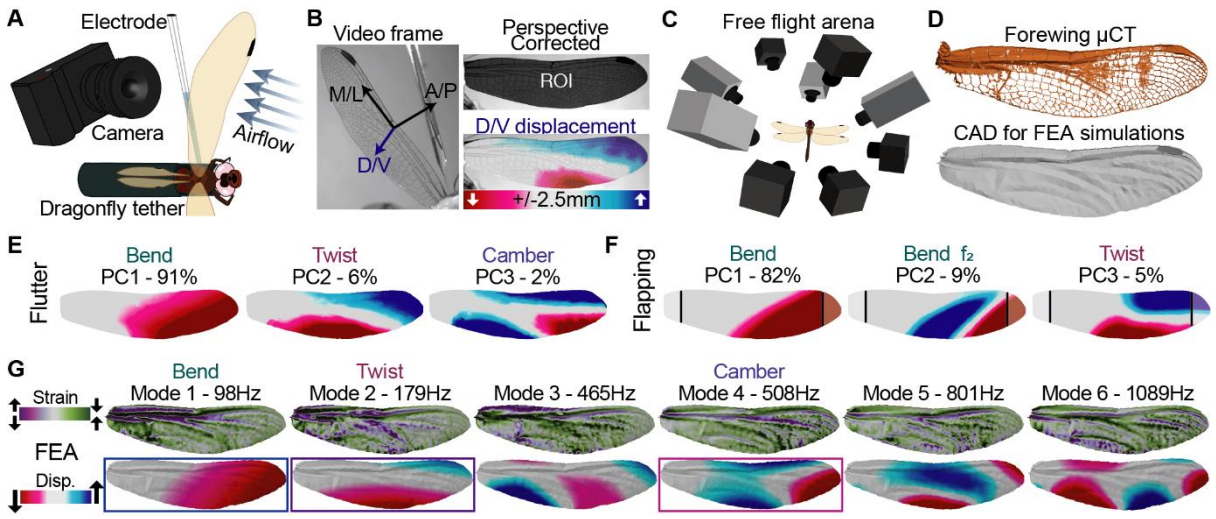

Figure 1: Wing morphing parameters

A) Wings were stimulated using controlled airflow while resulting deformations were filmed with a high-speed video camera at 1000 frames per second (fps) and the neural activity of the wing mechanosensory afferents were simultaneously recorded. B) Wings were filmed at an angle to maximize visualization of dorsoventral displacements (mediolateral and anterior-posterior displacements were negligible; see figure S1A). After perspective correction, DIC was used to measure displacements (example frame) and strain of the ROI. C) Nine synchronised high-speed cameras were used to captured free flight wing deformations at 500fps**.** D) A 3D external morphological model of a dragonfly forewing constructed by combining the wing venation network from stereoscopic 3D point cloud (via direct linear transformation, DLT) and the cross-section of the major longitudinal veins from μCT scanning. E) Displacement PCs of fixed wing airflow-induced deformations representing 99% of overall variability (N=5 animals, 14,000-49,000 frames/animal) F) Free flight flapping-induced deformations (base/tip interpolated from measured displacements) representing 96% of overall variability. G) FEA deformation modes (Strain: compressive-green, tensile-purple. Displacement: red-downward, blue-upward) ranked by frequency. Coloured boxes indicate key wing morphing parameters (see video S1).

Temporal receptive field: phase encoding

The frequency of periodic vibrations in biological structures contains information about the system's mechanical behaviour[39–42]. Since wing vibrations are periodic and we might reasonably assume that deformations are encoded, we first looked for phase information in afferent signals passing into the thoracic ganglia through the wing's anterior nerve. A template-matching custom spike sorting application[43] was used to identify individual units within each tethered recording; typically, recordings contained 1-4 distinguishable units. The patterns of deformation that activate individual units were identified by spike triggered averages (STA) using the PC reconstructions of displacement (Figure 2A). Multiple units often responded to the same patterns of deformations, but at different phases (Figure 2B). The phase of activation for these units was observed to shift depending on the displacement magnitude (Figure 2C). These responses enable the dragonflies to encode derived conditions: for example, bending mode magnitude at different points within the stroke cycle, or asymmetries between contralateral wings. Phase-locked units were classified using vector strength (VS; Figure S2) and units which were not phase-locked were not included in phase analysis (Figure 2C). Across trials, 1-2 large units dominated the overall activity of the recording and these units responded strongly and consistently to bend and twist at the wing's natural frequency and less strongly to camber.

Compared with simulated gliding (airflow-induced flutter while tethered), the deformation frequencies that occur during flapping flight are closer to wingbeat frequency (~40Hz), but the millisecond precision of these sensors is still necessary to detect flapping induced deformations accurately. Steering adjustments made throughout the stroke cycle are essential for manoeuvres, so to determine whether detectable changes in the deformation patterns occur within a single wingbeat, we measured wing bending and twist during free manoeuvring flight (Figure 2 D-G). We found that even relatively straight flight trajectories resulted in differences in the patterns of deformation across wing strokes. Though the wingbeat phase remained stable across wing strokes (Figure 2E), there were slight differences in stroke angle and bend amplitude (Figure 2E-F). During the roll turning manoeuvre (highlighted in red), there were obvious changes to the deformation patterns compared with straight flight, especially evident are the differences in the left and right forewing twist patterns (Figure 2G). These results demonstrate that the deformation modes we describe, are both temporally and behaviourally relevant for flapping flight manoeuvres and that such events are encoded by the wings' mechanosensor arrays.

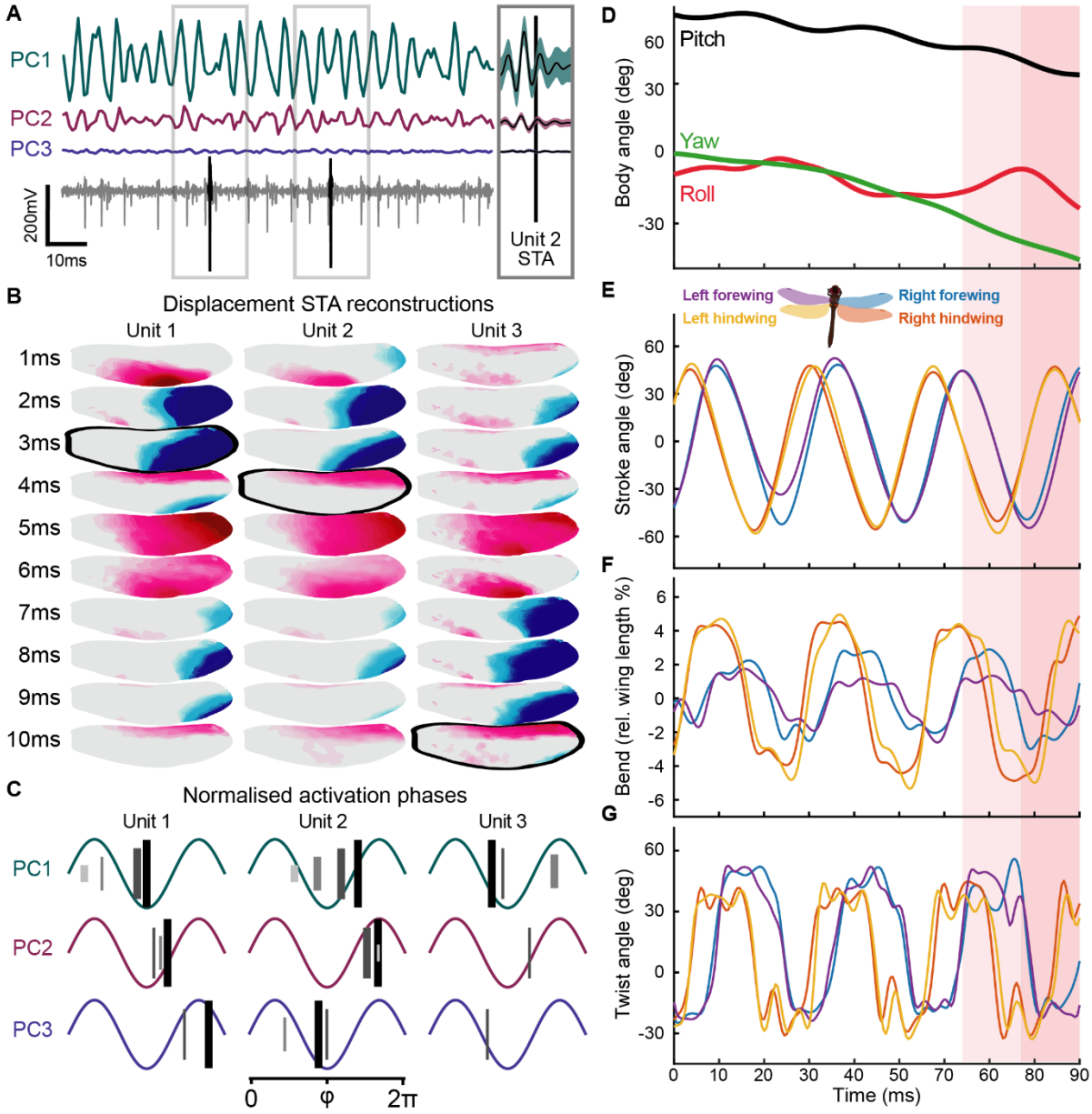

Figure 2: Phasic encoding.

A) PC scores and afferent spikes responding to airflow induced displacements were used to calculate STA for each unit (see figure S2A). Vertical black bars represent spike times for unit 2. B) Heatmap reconstructions of PC1-3 STA for airflow induced deformations with 4mm mean displacement. Each image represents a single frame (1ms). Images with black background show spike time for each unit. C) Activation timing of phase locked units for each PC (See figure S2B). Vertical bars show spike time relative to PC oscillation. Thick and thin bars represent strong (VS >0.6) and weak (0.6<VS<0.5) phase-locking respectively. Bar height and shade corresponds to displacement amplitude (1-4mm). Phase timing shifts with displacement amplitude. D) Body orientation over time of freely flying dragonfly (see video S2). Orientation is relatively straight for initial two wingbeats. Roll manoeuvre highlighted in red occurs during the third stroke cycle. E) Wing stroke angle showing relative wing timing across three wingbeats. F) Wing bend patterns change across wing strokes. G) Forewing twist pattern changes during roll manoeuvre.

<u>Perturbation detection</u>

Airflow induces consistent wing oscillations as a result of the structural and material properties of the wing. The natural frequency of the wing (Fourier transform dominant frequency of mean displacement of entire wing) across animals was 135+/-23Hz. Faster air speeds resulted in slightly higher frequencies (18.6+/-15.2Hz increase from 1-3m/s, N=5 animals). The dominant frequencies of the PCs were the same as the mean displacement frequency (Figure 3Ai). To determine whether deviations from airflow induced oscillation patterns are encoded by the wing sensors, we tested unnatural stimuli as a proxy for wing perturbations. Using a lever arm attached at the nodus, we vibrated the wing using either uniform white noise or a replay of airflow induced oscillations. To generate the replay stimuli, the nodus was tracked during airflow-induced oscillations and the same displacement was reproduced by the lever in the absence of any airflow. Vibration induced displacements were different from the natural airflow condition (Figure 3B); white noise vibration led to unique displacement PCs, whereas airflow playback PCs are still representative of bend, twist, and camber, but with different ranks and contributions compared with airflow PCs.

The frequency components of the wing's displacement are also different from the natural condition for both white noise and airflow playback, containing more and higher frequencies of motion at equivalent displacement amplitudes. Importantly, these differences were reflected in the neural signal. White noise vibration resulted in increased spike frequency, and recruitment of additional units at lower displacement amplitudes (Figure 3C). Airflow playback resulted in an intermediate response resembling airflow, but with a slight increase in extracellular activity.

To demonstrate whether the information encoded by these sensors is functionally relevant during flight behaviour, we ablated all wing surface sensors by lesioning the anterior wing nerves to see how this would affect the animals' ability to perform an energetic flight behaviour (take-off). The dragonfly take-off procedure has previously been described in detail and can be broken down into stereotypic components (Li *et al.* 2018). Here we focused on the first four full wingbeats, during which time the fore- and hindwings move in synchronous phase. Animals with ablated anterior nerves, were capable of flapping their wings normally but were generally unmotivated to take-off. Nerve ablated animals that did make take-off attempts tended not to gain as much elevation as their intact and sham counterparts (Figure S3A). Additionally, in cases where nerve ablated animals did demonstrate the ability to generate lift, we observed them abandoning their attempts once airborne and either gliding or falling to the ground (Video S1). For intact, sham, and ablated animals, there were no significant differences in wingbeat frequency (WBF) or in forewing-hindwing phase (Figures 3D) between each of the first four consecutive wingbeats measured within a condition, so individual wingbeats were pooled. There were no differences in forewing-hindwing phase across all conditions and no differences in WBF between intact and sham. However, nerve ablated animals did have significantly lower WBFs compared to both intact and sham animals (Figure 3D). These results demonstrate the necessity of anterior nerve sensory inputs for appropriate wing stroke frequency and the ability to generate and maintain adequate lift during take-off. They are also consistent with previous tethered flight experiments showing that the central nervous system contains all the neuronal machinery required to produce tethered flight but cutting off input from the periphery (including feedback information from the wings) results in patterns of action potentials that resemble flight activity, but at greatly reduced frequencies[44].

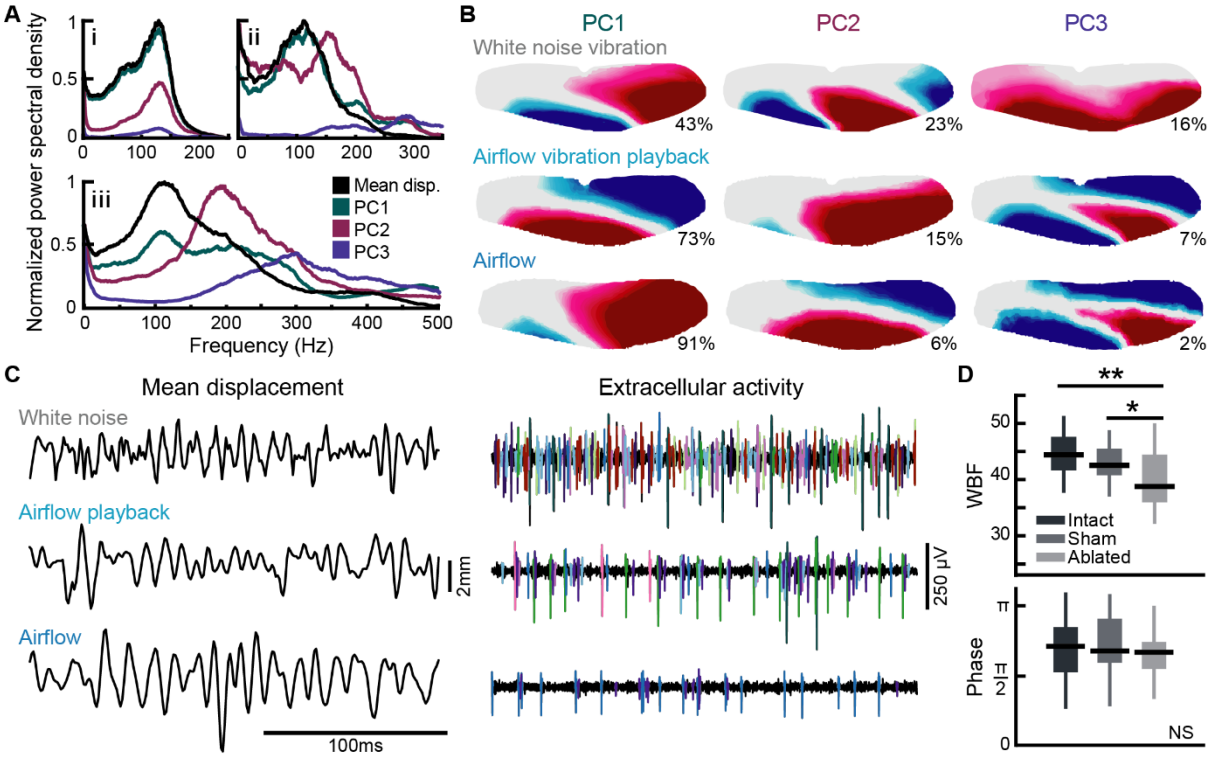

Figure 3: Deformation perturbations.

A) Smoothed displacement frequency components of mean displacement and airflow PCs (bend, twist, camber; see also Figure S4) for (i) airflow, (ii) airflow vibration playback, and (iii) white noise vibration stimuli. B) White noise vibrations result in unique displacement PCs. Airflow-induced and airflow playback vibration PCs are the same, but with different rank order (same colormap as Figure 1). C) White noise induced displacements (top) result in greatly increased extracellular activity and airflow playback (middle) result in moderately increased activity compared to airflow induced displacements (bottom). Different colors indicate different units. D) Ablated WBF was significantly lower than intact (P=0.00002) and sham (P=0.0024) conditions. There was no significant difference between intact and sham WBF, and no significant phase differences between all conditions (see table S1).

<u>Spatial receptive field: sensor localization</u>

To identify candidate sensors for the recorded units, we calculated the coherence between the activity of each unit and the displacement or strain within every spatial bin (pixel) across the wing surface (Figure 4A). We then plotted the peak coherence (Figure 4B) and the frequency at which it occurred (Figure 4C) for all bins. Airflow stimulation is inherently non-repeatable, so to estimate the information rate for each bin, we used the most conservative lower bound method[37]. Figure 4D shows the region of the wing where the measured displacements had the highest information rate for a single unit. The bins with the highest information rates (top 1-5%) were plotted for each of the recorded units within an animal for both displacement and strain measurements (Figure 4E). Estimates for regions of maximum information rate were calculated for multiple individuals (Figure 4F) and across animals; the identified regions corresponded to the same areas of the wing that our FEA modelling identified to experience the strongest strains associated with bend, twist, and camber (Figure 4G). Overlaying these regions with a map of wing strain sensors provides individual sensor (campaniform sensilla) candidates for the units recorded (Figure 4H). The highest sensor densities are found in the regions of the wing with the highest information, indicating that this is an optimal location for

detecting the strains associated with the most important wing deformation features. Information rates of dragonfly wing mechanosensors were found to be comparable to other spiking sensory systems (Figure 4I).

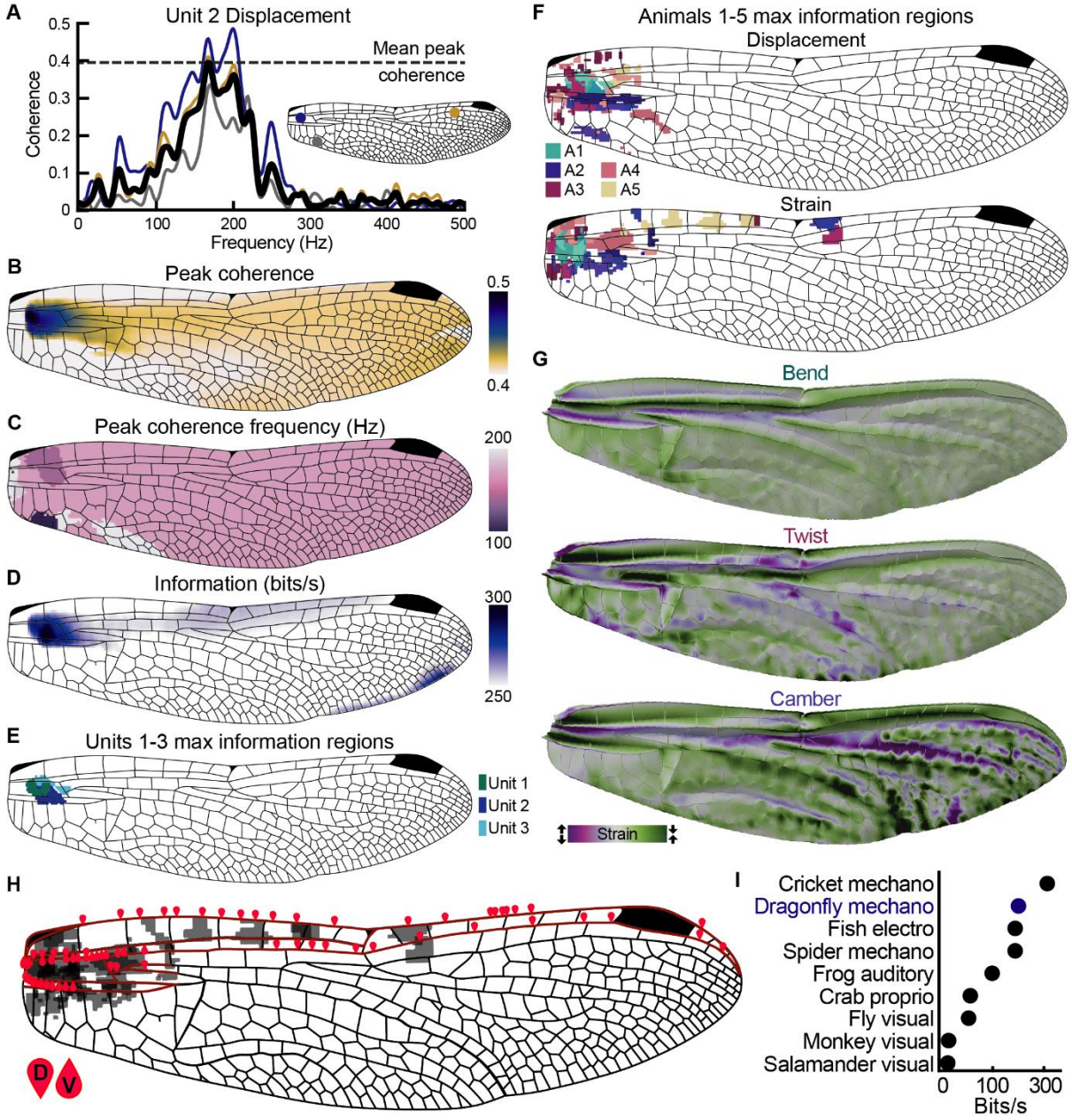

Figure 4: Sensor localisation.

A) Coherence between the activity of a single sensory unit and the displacement of the wing at three example spatial bins and the mean of all bins across the wing surface (black) between 0-500Hz. Unit 2 peak coherence for the mean of all bins is 171Hz. B) Peak coherence values of all bins. Darker regions show higher coherence. C) Frequencies at which the peak coherences shown in panel B occurred. For this unit, most peaks occur at 171Hz. D) Information rate of unit 2 estimated from coherence between 0-500Hz of all bins using the lower bound method. E) Wing regions with the highest displacement information rates for each of the recorded units previously shown in figure 2. The darkest region in D corresponds with the dark blue region shown here (unit 2). F) Wing regions with the highest displacement (top) and strain (bottom) information rates across animals (N=5). Colours correspond to individuals and shade variations show different units recorded from the same

individual. Data in A-E are from animal 1 (A1). G) FEA strain magnitude for key deformation modes (green-compressive, purple-tensile) showing regions of high strain. H) Locations of strain sensors (campaniform sensilla) on major veins. Dorsal and ventral denoted by tip direction. Shaded regions show high strain information rates from F. Sensors located in these regions represent likely candidates for the recorded units. I) Lower bound estimates of information rate across the recorded dragonfly wing mechanosensory units compared with other spiking sensory systems[45–53].

Discussion

Wings, in common with all structures, have spatial patterns and ranges of deformation that are constrained to finite modes and the natural range of spatial states can be simplified by dimensional reduction methods. Deformations, primarily composed of bending and twisting, represent the majority of the finite spatial patterns that wings experience across conditions. When wings are discretised to finite elements with sufficient geometric fidelity, the same patterns emerge in their primary modes (Figure 1). The wing's structural design drives deformations into predictable oscillatory patterns, such that the potential stimulus space is already reduced prior to any neurophysiological encoding. Encoding efficiency is further optimized by taking advantage of the regions of the wing that experience strong strains that are representative of the global motion. Strain maps of the key deformation modes show that the highest strains associated with bend, twist, and camber occur proximally, along the major wing veins, where the highest concentration of strain sensors is found. The feasibility of this being the optimal region for sensors to be placed is demonstrated further by the highest information rates for large amplitude phase locked units also falling within this locale. Dragonflies have hundreds of wing mechanosensors[27], but we focused on the units with large amplitude action potentials as they are more reliably identifiable across trials, although we note that larger amplitude signals do not necessarily contain more important information than spikes from smaller axons. However, larger signals likely originate from larger axons and will therefore reach the CNS more quickly for time-sensitive functions like those that are likely to arise during flight.

The timing of the phase-locked units described here is not as precise as some other systems, such as dipteran halteres, but this is not unexpected since dragonfly wings have additional degrees of freedom compared to halteres. Haltere and wing mechanics both limit their possible trajectories, but wings are exposed to additional, potentially less predictable, aerodynamic forces associated with actuation (generating lift). Despite the added complexity of the stimulus space, we show that wing sensors are still able to closely monitor the natural range of deformations using a simple phase-dependant encoding strategy. However, the range of deformations experienced during routine flight behaviour is not the *possible* range of deformation.

In 1948, J.W.S. Pringle observed that during normal haltere oscillations, mechanosensors are precisely timed with haltere motion, but perturbations from the natural trajectory resulted in afferents producing "a confused jumble of spikes"[54]. The jumble was disentangled 70 years later when it was demonstrated that during perturbations, spike timing precision is maintained, but spike phase may shift in different ways, depending on the sensor and the type of deviation[55]. For the sensors shown here, units recruited during perturbations overlap at a range of amplitudes lower than the phase locked sensors in what can only be described as "a confused jumble of spikes." There is no doubt that were every sensor recorded simultaneously, we might find a precise combination of sensor spike timings for every possible deviation from the natural wing state. It is also likely that these combinations would vary between individuals as a result of intraspecies morphological variations and also throughout development as wings harden or are damaged over time. Rather than relying solely on few high precision sensors, biological systems often use spatiotemporal sensor population codes to represent mechanosensory information[56]. In extreme conditions, where deformations outside the normal, natural range occur, additional sensors are required to represent any deformable structure. Though many sensors are metabolically costly to build and maintain, high sensor density is often attributed to redundancy rather than adaptability. The robustness of a system can certainly be improved through redundancy of sensors, but redundancy is not the only solution. Structural modifications resulting

from damage and development can also be compensated through population encoding strategies when they are flexible enough to adapt to change. So, while the high sensor density found on the wings of insects may be a result of redundancy, it is also possible that the complexity of the stimulus space simply requires many sensors.

Here, we have shown the first stages of information transformation that allow efficient representation of structural deformations. Investigations into downstream integration (Figure S5) will show how deformation pattern information is used to produce appropriate behavioural responses and control flight. We have demonstrated that morphology dictates and limits the range of the stimulus space and co-evolved sensor locations are optimised to reduce the redundancy of similar signals represented at multiple regions of the structure. The wing sensory system can monitor the wing's natural states with few sensors because the stimulus space is limited by morphology. Deviations from these states are detectable by a flexible population of additional sensors capable of many distinguishable temporal and spatial activation patterns associated with flight maneuverers and environmental perturbations.

Acknowledgements

The numerical simulation was supported by the Ansys Academic Research Partner program (MM).

Funding: Biotechnology and Biological Sciences Research Council, Grant/Award Numbers: BB/R002509/1 (to HTL), BB/R002657/1 (to RJB)

Others: The authors thank Daniel Ko, Sean Lim, Janka Kluga, Rui Zhou, and Myriam Uhrhan for their help with instrumentation. We thank Holger Krapp, Benjamin Campbell, and Samuel Fabian for their valuable discussion and feedback.

Author contributions

Conceptualization: HTL, RJB, AMY; Methodology: AMY, HK MM, SMW, RJB, HTL; Investigation: AMY, HK MM, SMW, RJB, HTL Visualization AMY, HK MM, SMW, RJB, HTL; Supervision: HTL, RJB; Writing: AMY, RJB, HTL

SUPPLEMENTAL

Methods

Electrophysiology:

The wing was stimulated using either an axial fan and airflow straightener to blow air across the wing at behaviourally relevant speeds (1-3m/s) and angles of attack (-/+20° & 0°; Figure S1) or with lever-arm vibrations using an Aurora Scientific 300C: Dual-Mode Muscle Lever. The lever was attached at the nodus, and vibration stimuli included uniform white noise or airflow playback - where the nodus was tracked and digitised using DLT DataViewer[57] during airflow stimulation and the same pattern of displacement was played back to replicate the natural wing motion in the absence of airflow. The wing was fixed at the hinge in natural gliding position using a 50/50 mixture paraffin and beeswax. The forewings naturally rest at a slight angle relative to the body which can vary slightly between animals, so airflow was aligned to the wingspan rather than to the body axis. Fixing the hinge reduces the region of interest to the wing surface mechanosensors and excludes internal proprioceptors, allowing only wing surface sensors to be activated. While fixing the wing in this way simulates gliding more closely than flapping flight, the natural range of deformation is restricted by the wing mechanics and does not change when the wing is articulated. Recordings where muscle

contractions occurred were easily identified and subsequently discarded. Hindwings were folded dorsally out of view of the camera and restricted with a folded strip of paper. To record the activity of wing mechanosensors, we performed a side entry dissection and removed a single layer of trachea to access the anterior wing nerve. A borosilicate glass suction electrode was pulled using a Sutter P-2000 Laser-Based Micropipette Puller, cut with a ceramic tile to match the diameter of each nerve (30-50μM), and used to record extracellularly from anterior nerve primary afferents. Anterior nerves receive inputs from all wing vein strain sensors (see figure 4H). The posterior wing nerve only receives inputs from the wing hinge, so posterior nerve recordings were not included here.

Deformations:

To identify the global motion patterns of the wing we aimed to represent the overall wing state with as few variables as necessary and sufficient. To measure local motion and strain, we filmed the deformations used to stimulate mechanosensors during electrophysiological recordings at 1000fps using a Chronos 2.1-HD camera (Kron Technologies Inc., Canada) and performed digital image correlation (DIC)[58] on the recorded video frames (Figure 1B). DIC requires a material's surface to be patterned, typically by painting with a splatter coat, however painting the wing would alter its mechanics and we found that the wing venation pattern alone was sufficient to extract displacement and strain. To accommodate electrode and stimulus while maximising visualisation of the largest deflections (dorso-ventral), animals were positioned on their side and angled upward at 40° with the camera placed approx. 20° behind the animal. Perspective correction, cropping, and contrast enhancement were performed on each frame prior to DIC analysis. Subset window sizes varied between animals depending on wing size and video quality but were typically 1% of the total wing size. Single camera measurements with perspective correction were sufficient to capture the same measured displacements as two camera 3D measurements (Figure S1A).

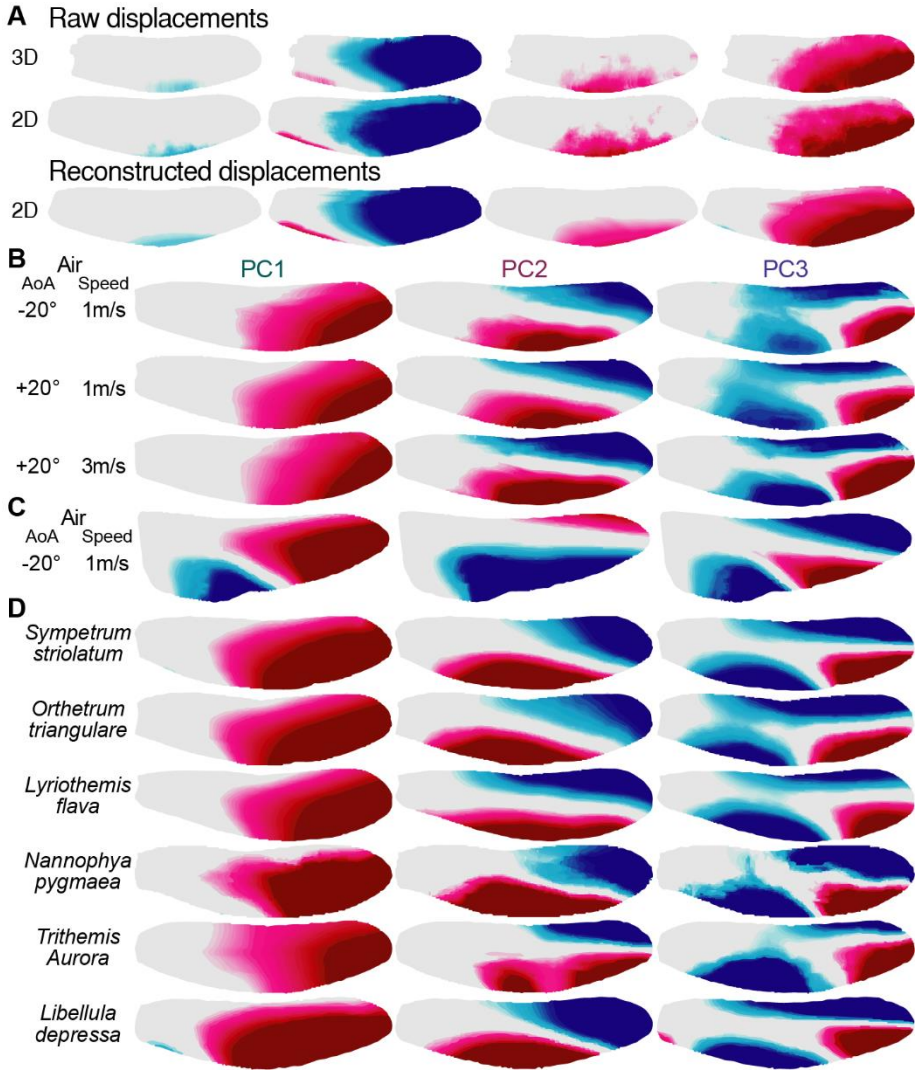

Figure S1: Wing displacement PCs.

A) Example frames of two camera 3D measurements of displacement magnitude (top), single camera dorso-ventral displacement measurements (middle) and PC displacement reconstruction (bottom). B) Angle of attack (AoA) and air speed do not influence PCs. Example PCs calculated from 7000 frames filmed at 1000fps. C) Hindwing PCs are similar to forewing PCs. PCs calculated from 5000 frames filmed at 1000fps. D) PCs are the same across dragonfly species tested. PCs calculated from 100-1000 frames filmed at 1000fps. Wings resized to equal wingspan and cord width for easier comparison.

<u>Finite Element Analysis:</u>

Combes and Daniel (2003) found that fluid-dynamic forces have a minimal effect on wing bending and concluded that overall deformation patterns are still sufficiently predicted when they are excluded from damped finite element models of insect wings.[59,60] A modal analysis simulation was performed for a dragonfly forewing model retaining realistic corrugation with Ansys Mechanical 2023 R2. The wing model geometry was constructed by combining the µCT scanning for a *S. striolatum* wing for vein cross-sections and the 3D venation from the direct linear transform (DLT) from a pair of stereo photos. See Fabian et al., 2022 for the details of the model construction method. The wing density (except for the pterostigma) was assumed to be 1200 kg/m3, while the pterostigma mass was set to be 9% of the total wing mass[61].

<u>Phase Analysis:</u>

Phase was calculated for each unit relative to PC scores by measuring the time between oscillation peaks and normalizing this to radians. The time point between peaks where the spike occurs is the phase value in radians. Phase-locked units were identified by calculating vector strength (VS; see Eq.1). Units with VS>0.6 were considered phase locked and VS between 0.5-0.6 were classified as weakly phase locked.

Equation 1: $$Vector\ strength = \frac{1}{N}\sqrt{\left(\sum_i \cos\theta_i{}^2\right) + \left(\sum_i \sin\theta_i{}^2\right)}$$

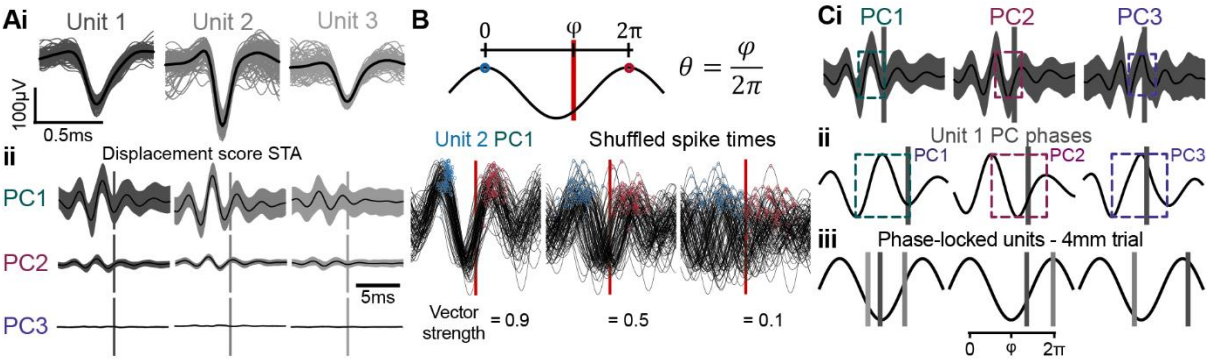

Figure S2: Phase measurements.

A) Sorted units shown in Figure 2 (i) and their associated PC STAs (ii). B) Phase (θ) is calculated by measuring the relative time (φ) between oscillation peaks normalized to radians. Phase-locked units are identified by calculating vector strength (VS; see Eq.1). Units with VS above 0.5 are classified as phase locked. C) Unit 1 phase (vertical bars) relative to PC score STAs (i) normalised to radians (ii). All phase locked units from airflow induced deformations with 4mm mean displacement (iii; see also Figure 2).

<u>Nerve ablations:</u>

Male *S. striolatum* were collected from artificial ponds at Imperial College London Silwood Park campus. Animals were kept at 7°C prior to experiments and restrained on a 13°C Peltier during surgery. Animals were subjected to either a sham surgery where the anterior nerves were exposed but kept intact or an ablation surgery where the anterior nerves were lesioned. After surgery, parafilm was used to cover the incision site and secured with beeswax. Animals were allowed 20-30 minutes recovery time and were screened prior to and after surgery to ensure they were healthy and capable of sustained lift in free flight. This was defined by whether when manually dropped inside the behaviour arena, individuals were able to navigate to the ceiling or wall at or above the initial drop height. To encourage animals to take off, they were placed on a 75x75 mm platform with a Peltier heating element underneath. The Peltier warmed to a maximum of 59°C over 1.5 minutes. Take-offs were filmed at 1000fps using two Chronos 2.1-HD cameras (Kron Technologies Inc., Canada) and digitised using DLT DataViewer[57]. Data were non-normally distributed, so comparisons were made using Kruskal-Wallice (WBF) or Multi-sample test for equal median directions (phase) with Bonferroni correction for six comparisons (Table S1)[62].

Previous work in locust[63,64] and hawkmoth[65] has demonstrated the influence of hindwing mechanosensory (tegula) inputs on forewing motor control. In these insects, the tegula plays an important role in the generation of rhythmic flight motor patterns. A similar mechanism in dragonflies could explain how forewing nerve ablated animals are still able to maintain synchrony between the fore- and hindwings, albeit at a lower frequency. Tegula have not previously been described in dragonflies. However, we identified a tegula-like structure called the ‘tegula complex’ which

comprises a hair plate and campaniform sensilla field (Figure S5D). In Locusts, hindwing tegula play a larger role in the production of flight motor patterns than the forewing tegula[66] and in all experimental conditions shown here, the hindwing nerves (which contain afferents from the hindwing tegula complex) were kept intact. While the hindwing mechanosensors are almost certainly involved in forewing motor control, we are unable to demonstrate how ablation of these inputs compares with forewing nerve ablation during takeoff behaviour because hindwing nerve ablation requires a more invasive surgery with low likelihood of recovery. Further, the recorded mechanosensors did not include afferents from the tegula complex as the wing was fixed and these sensors are located at the wing hinge where they are only activated at the peak of the upstroke and not involved in deformation sensing.

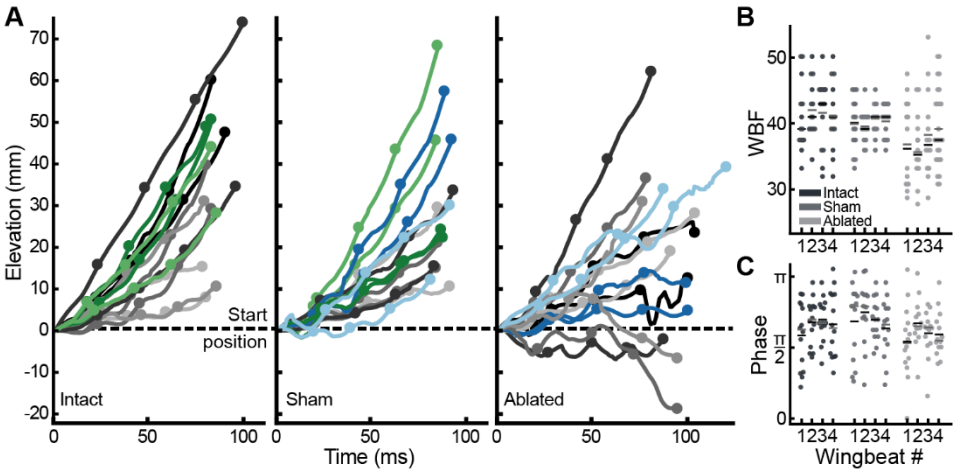

Figure S3: Nerve ablation.

A) Takeoff elevation over the first four wingbeats. Different shades represent different animals. Circles mark time of forewing downstroke. N=7 animals, 2 trials per condition. Two animals appear in both intact and sham (green) and two in both sham and ablated (blue). B) No significant differences in WBF between wingbeats within each condition. Grey and black bars show mean and median respectively. Ablated WBF significantly lower than intact (P=0.00002) and sham (P=0.0024). No significant difference between intact and sham WBF. C) No significant differences in the hindwing phase relative to the forewing between wingbeats within each condition. No significant differences between all conditions. Data resolution results from video frame rate (1000fps).

Table S1: Nerve ablation multiple comparisons P values.

Comparison	Between wingbeats			Between conditions		
	Intact	Sham	Ablate	Intact vs. sham	Sham vs. ablate	Intact vs. ablate
Phase	0.58	0.47	0.75	0.058	0.023	0.57
WBF	0.94	0.63	0.49	0.016	0.0024*	0.000017**

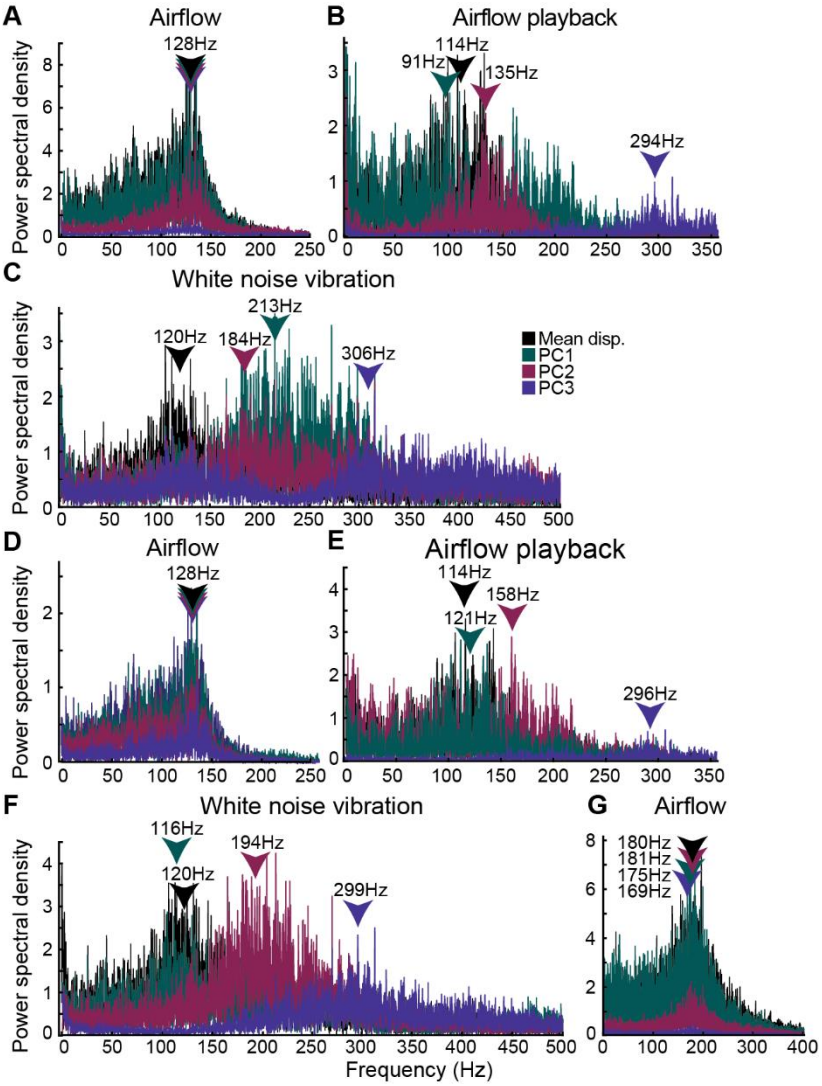

Figure S4: Displacement frequency components.

Mean displacement and PC score frequency components for airflow (A) airflow vibration playback (B), and white noise vibration. D-E) Mean displacement and PC scores calculated for PCs extracted from different stimulus type. D) White noise PC scores measured within airflow stimulus E) Airflow PC scores (bend, twist, camber) measured within airflow playback stimulus. F) Airflow PC scores (bend, twist, camber) measured within white noise G) Mean displacement and PC score frequency components for animal shown in Figure 2.

<u>Neural information:</u>

The magnitude-squared coherence (C_{xy}) was estimated between each unit's activity (x) and the displacement or strain change from baseline of each bin (y) as a function of their power spectral densities, Pxx and Pyy, and cross power spectral density, Pxy between 0 and 500Hz[67]. Numerical approximation error was reduced by increasing the number of segments used. Averaging across many segments decreases the frequency resolution, which is reflected in Figure 4A where the frequencies measured appear smoothed. This can also result in a loss of information for slowly varying components of the signal; however, these components are not behaviourally relevant as the forces acting on the wing during flight are not slowly varying. Coherence calculations using few segments did produce similar spatial maps, but also amplified DIC measurement errors resulting in unreliable coherence and information rate estimates.

Equation 2: $$C_{xy} = \frac{|P_{xy}|^2}{P_{xx}P_{yy}}$$

Turbulent airflow stimulation is not repeatable, so the more conservative lower bound method was used to estimate information rate (I) in bits/s from coherence[37,68]. Very large displacements result in larger error during DIC analysis due to motion blur, so outliers were removed prior to coherence estimation in these cases. High information regions were defined as the bins with information rates within the top 1-5% (depending on the number of outliers removed). Outliers only occurred along the lateral trailing edge of the wing where sensor density is far lower, likely because this region is more prone to damage[19,69].

Equation 3: $$I = -\int_{0Hz}^{500Hz} \log_2\left(1 - C_{xy}\right) df$$

<u>Imaging:</u>

See Fabian et al., 2022 for neural imaging and sensor distribution mapping protocols.

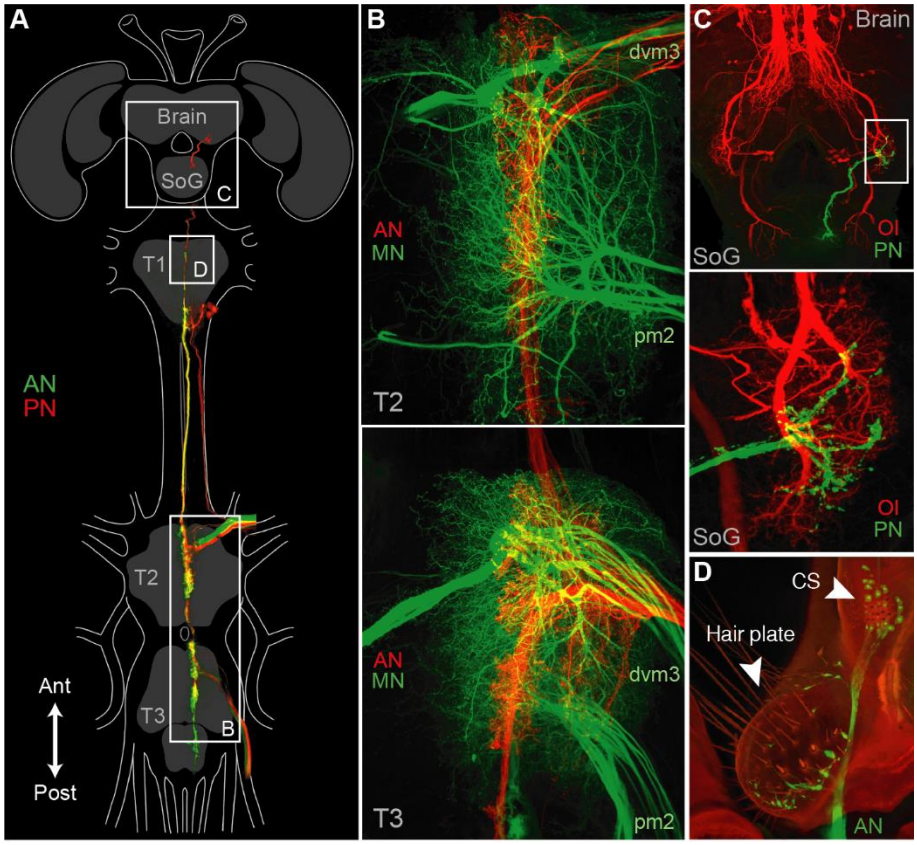

Figure S5: Wing mechanosensor neuroanatomy.

A) Anterior (AN) and posterior (PN) wing nerves project ipsilaterally within T2 & T3. PN projects to T1 and brain (panel C) and a subset of AN afferents from the tegula complex (panel D) project to T1. B) AN projects to wing motor neurons (MN) dvm3 (pronation) and pm2 (anti-overpronation. C) PN projections to secondary ocellar interneurons (OI) in the posterior deutocerebrum. D) Hair plate and CS comprise the tegula complex.

<u>Free flight kinematics:</u>

S. striolatum were filmed taking off from a vertical perch using using nine high-speed cameras (five Photron AX200 and four Photron SA3, Photron Ltd) recording at 2000fps and 1024 x 1024px. Sequences were trimmed to exclude time when the body was within approximately one body length of

the perch and all four wings were engaged in stereotypical flapping flight. A voxel-carving method used to measure the six degrees of freedom of the body and wingtip spherical coordinates[70]. Fifth order polynomials were fitted to the voxels corresponding to the leading and trailing edge of the wing (from 10% to 90% wing length), which were then transformed into a wing-root axis system, aligned with the basal twist of the wing. Wing deformations (Figure 1G) were then calculated by fitting a 80x50 point surface to the leading and trailing edge polynomials. In total, 14 sequences were processed, including 99 wingbeats (pooling left and right forewings).

Videos

Video S1: Global displacement of FEA modes.

Video S2: Free flight kinematics.

Video S3: Example intact vs. nerve ablated takeoff.
Wingbeat frequency decreases after nerve ablation and animals often abandon takeoff attempts once airborne.

References:

1. Marshall, K. L. & Lumpkin, E. A. The Molecular Basis of Mechanosensory Transduction. *Adv. Exp. Med. Biol.* **739**, 142–155 (2012).
2. Makarova, A. A., Polilov, A. A. & Chklovskii, D. B. Small brains for big science. *Curr. Opin. Neurobiol.* **71**, 77–83 (2021).
3. Song, F., Yan, Y. & Sun, J. Review of insect-inspired wing micro air vehicle. *Arthropod Struct. Dev.* **72**, 101225 (2023).
4. Bergmann, J. B., Moatsou, D., Steiner, U. & Wilts, B. D. Bio-inspired materials to control and minimise insect attachment. *Bioinspir. Biomim.* **17**, 051001 (2022).
5. Díaz-García, L., Latham, B., Reid, A. & Windmill, J. Review of the applications of principles of insect hearing to microscale acoustic engineering challenges. *Bioinspir. Biomim.* **18**, 051002 (2023).
6. Holden-Dye, L. & Walker, R. J. Invertebrate models of behavioural plasticity and human disease. *Brain Neurosci. Adv.* **2**, 2398212818818068 (2018).
7. O'Carroll, D. C., Bidweii, N. J., Laughlin, S. B. & Warrant, E. J. Insect motion detectors matched to visual ecology. *Nature* **382**, 63–66 (1996).

8. Bennet-Clark, H. C. 8. Songs and the Physics of Sound Production. in *8. Songs and the Physics of Sound Production* 227–261 (Cornell University Press, 2019). doi:10.7591/9781501745904-010.
9. Schildberger, K. & Hörner, M. The function of auditory neurons in cricket phonotaxis. *J. Comp. Physiol. A* **163**, 621–631 (1988).
10. Fayyazuddin, A. & Dickinson, M. H. Haltere afferents provide direct, electrotonic input to a steering motor neuron in the blowfly, Calliphora. *J. Neurosci. Off. J. Soc. Neurosci.* **16**, 5225–5232 (1996).
11. Webb, B., Harrison, R. R. & Willis, M. A. Sensorimotor control of navigation in arthropod and artificial systems. *Arthropod Struct. Dev.* **33**, 301–329 (2004).
12. Huston, S. J. & Krapp, H. G. Nonlinear Integration of Visual and Haltere Inputs in Fly Neck Motor Neurons. *J. Neurosci.* **29**, 13097–13105 (2009).
13. Longden, K. D., Muzzu, T., Cook, D. J., Schultz, S. R. & Krapp, H. G. Nutritional State Modulates the Neural Processing of Visual Motion. *Curr. Biol.* **24**, 890–895 (2014).
14. Bender, J. A. & Dickinson, M. H. A comparison of visual and haltere-mediated feedback in the control of body saccades in Drosophila melanogaster. *J. Exp. Biol.* **209**, 4597–4606 (2006).
15. Dahake, A., Stöckl, A. L., Foster, J. J., Sane, S. P. & Kelber, A. The roles of vision and antennal mechanoreception in hawkmoth flight control. *eLife* **7**, e37606 (2018).
16. Rien, D., Kern, R. & Kutz, R. Octopaminergic modulation of a fly visual motion-sensitive neuron during stimulation with naturalistic optic flow. *Front. Behav. Neurosci.* **7**, (2013).
17. Pringle, J. W. S. Proprioception In Insects: I. A New Type Of Mechanical Receptor From The Palps Of The Cockroach. *J. Exp. Biol.* **15**, 101–113 (1938).
18. Shyy, W. *et al.* Recent progress in flapping wing aerodynamics and aeroelasticity. *Prog. Aerosp. Sci.* **46**, 284–327 (2010).
19. Rudolf, J., Wang, L.-Y., Gorb, S. N. & Rajabi, H. On the fracture resistance of dragonfly wings. *J. Mech. Behav. Biomed. Mater.* **99**, 127–133 (2019).
20. Bomphrey, R. J., Nakata, T., Henningsson, P. & Lin, H.-T. Flight of the dragonflies and damselflies. *Philos. Trans. R. Soc. Lond. B. Biol. Sci.* **371**, 20150389 (2016).

21. Darvizeh, M., Darvizeh, A., Rajabi, H. & Rezaei Mojdehi, A. Free vibration analysis of dragonfly wings using finite element method. *Int. J. Multiphysics* **3**, 101–110 (2009).
22. Rajabi, H. *et al.* Effect of microstructure on the mechanical and damping behaviour of dragonfly wing veins. *R. Soc. Open Sci.* **3**, 160006 (2016).
23. Lietz, C., Schaber, C. F., Gorb, S. N. & Rajabi, H. The damping and structural properties of dragonfly and damselfly wings during dynamic movement. *Commun. Biol.* **4**, 1–14 (2021).
24. Li, Q., Zheng, M., Pan, T. & Su, G. Experimental and Numerical Investigation on Dragonfly Wing and Body Motion during Voluntary Take-off. *Sci. Rep.* **8**, 1011 (2018).
25. Rajabi, H. *et al.* A comparative study of the effects of constructional elements on the mechanical behaviour of dragonfly wings. *Appl. Phys. A* **122**, 19 (2015).
26. Sunada, S., Zeng, L. & Kawachi, K. The Relationship Between Dragonfly Wing Structure and Torsional Deformation. *J. Theor. Biol.* **193**, 39–45 (1998).
27. Fabian, J. *et al.* Systematic characterization of wing mechanosensors that monitor airflow and wing deformations. *iScience* **25**, 104150 (2022).
28. Arriola-Rios, V. E. *et al.* Modeling of Deformable Objects for Robotic Manipulation: A Tutorial and Review. *Front. Robot. AI* **7**, 82 (2020).
29. Nadon, F., Valencia, A. J. & Payeur, P. Multi-Modal Sensing and Robotic Manipulation of Non-Rigid Objects: A Survey. *Robotics* **7**, 74 (2018).
30. Rus, D. & Tolley, M. T. Design, fabrication and control of soft robots. *Nature* **521**, 467–475 (2015).
31. Montagnat, J., Delingette, H. & Ayache, N. A review of deformable surfaces: topology, geometry and deformation. *Image Vis. Comput.* **19**, 1023–1040 (2001).
32. Gherlone, M., Cerracchio, P. & Mattone, M. Shape sensing methods: Review and experimental comparison on a wing-shaped plate. *Prog. Aerosp. Sci.* **99**, 14–26 (2018).
33. Ma, Z., Choi, J. & Sohn, H. Structural displacement sensing techniques for civil infrastructure: A review. *J. Infrastruct. Intell. Resil.* **2**, 100041 (2023).
34. Wang, X. *et al.* Recent Progress in Electronic Skin. *Adv. Sci.* **2**, 1500169 (2015).

35. Chen, L. *et al.* Spike timing–based coding in neuromimetic tactile system enables dynamic object classification. *Science* **384**, 660–665 (2024).
36. Reich, D. Spikes: Exploring the Neural Code. *Netw. Comput. Neural Syst.* **8**, 008 (1997).
37. Borst, A. & Theunissen, F. E. Information theory and neural coding. *Nat. Neurosci.* **2**, 947–957 (1999).
38. Koehler, C., Liang, Z., Gaston, Z., Wan, H. & Dong, H. 3D reconstruction and analysis of wing deformation in free-flying dragonflies. *J. Exp. Biol.* **215**, 3018–3027 (2012).
39. Wilson, A. M., McGuigan, M. P., Su, A. & van Den Bogert, A. J. Horses damp the spring in their step. *Nature* **414**, 895–899 (2001).
40. Ishizaka, K. & Flanagan, J. L. Synthesis of voiced sounds from a two-mass model of the vocal cords. *Bell Syst. Tech. J.* **51**, 1233–1268 (1972).
41. Hudspeth, A. J. How the ear's works work. *Nature* **341**, 397–404 (1989).
42. Cade, W. Acoustically Orienting Parasitoids: Fly Phonotaxis to Cricket Song. *Science* **190**, 1312–1313 (1975).
43. Ko, D. & Lin, H.-T. NBits-Dragonsort. Neuromechanics & Bioinspired Technologies (NBits) Lab (2024).
44. Simmons, P. J. The neuronal control of dragonfly flight. (1977) doi:10.25911/5d7783acf1631.
45. Eeckman, F. H. *Analysis and Modeling of Neural Systems*. (Springer US, 1992).
46. Clague, H., Theunissen, F. & Miller, J. P. Effects of adaptation on neural coding by primary sensory interneurons in the cricket cercal system. *J. Neurophysiol.* **77**, 207–220 (1997).
47. Warland, D. K., Reinagel, P. & Meister, M. Decoding visual information from a population of retinal ganglion cells. *J. Neurophysiol.* **78**, 2336–2350 (1997).
48. Wessel, R., Koch, C. & Gabbiani, F. Coding of time-varying electric field amplitude modulations in a wave-type electric fish. *J. Neurophysiol.* **75**, 2280–2293 (1996).
49. Juusola, M. & French, A. S. The Efficiency of Sensory Information Coding by Mechanoreceptor Neurons. *Neuron* **18**, 959–968 (1997).

50. Theunissen, F., Roddey, J. C., Stufflebeam, S., Clague, H. & Miller, J. P. Information theoretic analysis of dynamical encoding by four identified primary sensory interneurons in the cricket cercal system. *J. Neurophysiol.* **75**, 1345–1364 (1996).
51. Buračas, G. T., Zador, A. M., DeWeese, M. R. & Albright, T. D. Efficient Discrimination of Temporal Patterns by Motion-Sensitive Neurons in Primate Visual Cortex. *Neuron* **20**, 959–969 (1998).
52. DiCaprio, R. A., Billimoria, C. P. & Ludwar, B. C. Information rate and spike-timing precision of proprioceptive afferents. *J. Neurophysiol.* **98**, 1706–1717 (2007).
53. Bialek, W., Rieke, F., De Ruyter Van Steveninck, R. R. & Warland, D. Reading a Neural Code. *Science* **252**, 1854–1857 (1991).
54. Pringle, J. W. S. The Gyroscopic Mechanism of the Halteres of Diptera. *Philos. Trans. R. Soc. Lond. Ser. B* **233**, 347–384 (1948).
55. Yarger, A. M. & Fox, J. L. Single mechanosensory neurons encode lateral displacements using precise spike timing and thresholds. *Proc. Biol. Sci.* **285**, 20181759 (2018).
56. Aiello, B. R. *et al.* Spatial distribution of campaniform sensilla mechanosensors on wings: form, function, and phylogeny. *Curr. Opin. Insect Sci.* **48**, 8–17 (2021).
57. Hedrick, T. L. Software techniques for two- and three-dimensional kinematic measurements of biological and biomimetic systems. *Bioinspir. Biomim.* **3**, 034001 (2008).
58. Blaber, J., Adair, B. & Antoniou, A. Ncorr: Open-Source 2D Digital Image Correlation Matlab Software. *Exp. Mech.* **55**, 1105–1122 (2015).
59. Combes, S. A. & Daniel, T. L. Into thin air: contributions of aerodynamic and inertial-elastic forces to wing bending in the hawkmoth *Manduca sexta*. *J. Exp. Biol.* **206**, 2999–3006 (2003).
60. Baroth, E. *et al.* IVHM (Integrated Vehicle Health Management) techniques for future space vehicles. in *37th Joint Propulsion Conference and Exhibit* (American Institute of Aeronautics and Astronautics). doi:10.2514/6.2001-3523.
61. Åke Norberg, R. The pterostigma of insect wings an inertial regulator of wing pitch. *J. Comp. Physiol.* **81**, 9–22 (1972).

62. Fisher, N. I. *Statistical Analysis of Circular Data*. (Cambridge University Press, Cambridge, 1993). doi:10.1017/CBO9780511564345.
63. Gettrup, E. Sensory Regulation of Wing Twisting in Locusts. *J. Exp. Biol.* **44**, 1–16 (1966).
64. Wolf, H. The Locust Tegula: Significance for Flight Rhythm Generation, Wing Movement Control and Aerodynamic Force Production. *J. Exp. Biol.* **182**, 229–253 (1993).
65. Frye, M. A. Effects of stretch receptor ablation on the optomotor control of lift in the hawkmoth Manduca sexta. *J. Exp. Biol.* **204**, 3683–3691 (2001).
66. Büschges, A., Ramirez, J.-M. & Pearson, K. G. Reorganization of sensory regulation of locust flight after partial deafferentation. *J. Neurobiol.* **23**, 31–43 (1992).
67. Kay, S. M. *Modern Spectral Estimation: Theory and Application*. (Prentice Hall, Englewood Cliffs, N.J., 1988).
68. Shannon, C. E. A mathematical theory of communication. *Bell Syst. Tech. J.* **27**, 379–423 (1948).
69. Rajabi, H., Schroeter, V., Eshghi, S. & Gorb, S. N. The probability of wing damage in the dragonfly Sympetrum vulgatum (Anisoptera: Libellulidae): a field study. *Biol. Open* **6**, 1290–1293 (2017).
70. Walker, S. & Taylor, G. A semi-empirical model of the aerodynamics of manoeuvring insect flight. *J. R. Soc. Interface* **18**, 20210103 (2021).